npj | Flexible Electronics

www.nature.com/npjflexelectron

ARTICLE OPEN

Check for updates

On-skin ultrathin and stretchable multifunctional sensor for smart healthcare wearables

Shipeng Zhang[1,2], Ashok Chhetry[1,2], Md. Abu Zahed[1], Sudeep Sharma[1], Chani Park[1], Sanghyuk Yoon[1] and Jae Y. Park[1]✉

The flexible and stretchable multifunctional sensors for the precise monitoring of the human physiological health indicators is an emerging requirement of next-generation electronics. However, the integration of multifunctional sensors into a common substrate for simultaneous detection of such signals without interfering with each other is the most challenging work. Here, we propose MXene-$Ti_3C_2T_x$ and 3, 4-ethylene dioxythiophene (EDOT) deposited on laser-induced graphene (LIG/MXene-$Ti_3C_2T_x$@EDOT) composite-based flexible and stretchable multifunctional sensors for strain, temperature, and electrocardiogram (ECG) monitoring. In-situ electrophoretic deposition (EPD) of MXene-$Ti_3C_2T_x$@EDOT composite into LIG outperforms high strain sensitivity of 2,075, temperature coefficient of resistance (TCR) of 0.86%, and low skin-contact impedance. The sensor platform is integrated into an ultrathin and highly resilient polystyrene-*block*-poly(ethylene-*ran*-butylene)-*block*-polystyrene (SEBS). Finally, we demonstrate on-site detection of human body-induced deformations and physiological health indicators, such as temperature and ECG. The proposed approach paves a promising route to future wearables for smart skin and healthcare applications.

npj Flexible Electronics (2022)6:11 ; https://doi.org/10.1038/s41528-022-00140-4

INTRODUCTION

The development of wearable and flexible multifunctional sensors has attracted extensive attention in smart biomedical and healthcare applications. The real-time monitoring of a person's physiological status, such as pulse rate, body temperature, and electrocardiogram (ECG) assists medical personnel in the early prediction and diagnosis of heart diseases or abnormal body conditions[1,2]. As a core component of wearable devices, flexible and stretchable multifunctional sensors have good application prospects in health-status monitoring[2], electronic-skin (e-skin)[3,4], and human-machine interface[5,6]. Although intensive research efforts have been done in the fabrication of multifunctional sensors, the challenges of seamless integration of such sensors into a stretchable platform restrict the wearability and selectivity of multiple stimuli. In addition, identifying a common functional material responsive to a variety of stimuli is also a key constraint for multimodal wearable electronics.

To date, there have been several reports on the flexible strain and temperature sensors using metallic materials (particles[7–11], nanowires[12,13], and nanosheets[14] and carbon materials (carbon black[15], carbon nanotubes[14,16], graphene[3,17,18], and ionic liquids[6]. Organic nanomaterials, such as poly(3,4- ethylenedioxythiophene)-poly(styrenesulfonate) (PEDOT: PSS)[19] and polyaniline-based hydrogels[4] are also alternative materials for temperature sensors. Although some of the results are impressive, there is a compromise between most essential parameters of the temperature sensors *viz*. temperature coefficient of resistance (TCR) and physiological temperature range. In addition, the electrical performances of most of the thermistors based on intrinsically stretchable materials are influenced by strains, resulting in the unstable response; thus cannot measure multiple parameters simultaneously[20]. Nevertheless, the crucial performance parameters of such sensors, sensitivity, and working range, have not been achieved simultaneously because of the specific structure of the functional materials. For instance, 0D materials, such as nanoparticles tend to separate from each other during strain because of their short aspect ratio, thereby limiting the sensing range[8]. Moreover, 1D materials, such as nanowires and nanotubes have relatively a wide sensing range but exhibit low sensitivity because their high aspect ratio makes them easily entangle with each other, and the resistance change is not apparent even under large deformations[9,21,22]. In 2D materials, an effective slippage cannot be generated under tensile stress, causing large cracks that break the conductive pathways, thereby limiting the sensitivity of the sensor. Such devices with 2D materials can work only within a very narrow sensing range because of the close stack and interaction between adjacent sheets[23,24]. In addition, an efficient wearable electrode is crucial for accurately recording biopotential signals, especially in the case of continuous monitoring of inconspicuous heart diseases and rehabilitation in daily life. As such, the conformal contact between the skin and electrode is essential for obtaining precise acquisition of biosignals[25]. Such devices require to be ultrathin and need to have seamless contact with the human body to be comfortable to wear. At present, Ag/AgCl gel electrodes are predominant in a clinical setting to obtain surface bio-potentials, but prone to signal degradation in the long run of continuous monitoring due to the volatilization of the liquid in gel electrolyte and causes skin allergies/irritation[26]. In particular, metal films, such as gold (Au) can have low contact impedance but not stretchable; as a result, high noise can be observed on the biopotential signals, resulted from curved body surfaces and/or due to body movements. Apart from this, PEDOT:PSS electrodes are also widely studied in recent years in bioelectronics due to easy processing and biocompatibility[26,27]. However, the limited flexibility of the substrate materials results in poor contact thereby showing higher impedances. Therefore, choosing a suitable functional material, geometric engineering, and efficient fabrication technique is essential for the performance enhancement of the emerging class of flexible and stretchable electronics.

[1]Department of Electronic Engineering, Kwangwoon University, 447-1 Wolgye-dong, Nowon-gu, Seoul 01897, Republic of Korea. [2]These authors contributed equally: Shipeng Zhang, Ashok Chhetry. ✉email: jaepark@kw.ac.kr

Alternatively, MXene-$Ti_3C_2T_x$, a recently augmented material of 2D materials exhibits many excellent properties, such as electrical conductivity and bending strengths, which are comparable to those of graphene. Likewise, the oxidation resistance and electron irradiation resistance of MXenes are superior to those of graphene. In addition, MXenes prepared by chemical liquid phase etching usually contain highly hydrophilic functional groups (−OH, −F, and −O) thus can easily be modified, and are widely used in energy storage[28,29], catalysis[30], and electromagnetic shielding[31]. Therefore, MXene has gradually gained more attention in the field of flexible electronics due to its good electrical conductivity and mechanical flexibility. Exploiting 2D materials, such as MXene-$Ti_3C_2T_x$ with a second material having different dimensions can overcome the limitation of stress dispersion, which produces larges cracks in 2D materials, benefiting the stretchability of the sensors[14,32].

The approach of integrating the multitude of sensors into a common substrate is straightforward. Such sensors can overcome the existing limitations of simultaneous detection of multiple parameters without interference. Although extensive research has been done in multifunctional sensors, consolidation of individual single parameter sensors into a common substrate leads to a bigger sensor size, subsiding the wearing comfort[33,34]. However, the need for ultrathin, lightweight, and mechanically flexible, and stretchable multifunctional sensor requires an appropriate sensor design and choice of good functional material to respond to each stimulus[35]. In addition, the successful detection of each stimulus without interfering with each other is of profound importance to fulfill the requirement of multifunctional sensors. For example, a flexible multifunctional sensor developed by spraying a mixture of carbon black and reduced graphene oxide for strain, humidity, temperature, and pressure with a single layer is sensitive to all kinds of stimulus[36]. In such multifunctional sensors, the integration of multiple sensors in a layer-by-layer fashion is also hindered by the nature of the paper-based substrate layer. Recently, Kaidarova, A. et al. developed double-sided LIG multifunctional sensors for body movements of marine animals in the Red sea[37]. However, animal-attached bending sensors require sufficient GF (1.16) and stretchability (~10%) to conformably attach and sense the speed of marine animals. In addition, the temperature of the Red sea (warm up to 36 °C), and saltiest often cause interference in signal measurement and are prone to corrosion causing device failure.

In this regard, ultrathin, lightweight, and mechanically flexible and stretchable multifunctional sensor with high selectivity of multiple stimuli is the key design considerations[34,35]. Therefore, significant effort has been devoted to the development of skin-friendly sensors into a flexible and stretchable platform that can measure a full range of human-body-induced motions, temperature, and ECG signals.

In this study, we report multifunctional sensors integrated into a stretchable substrate for the simultaneous measurement of strain, temperature, and ECG without interfering with each other. The heterogeneity of sensing ability of the three different stimuli is enabled by a single composite material obtained by the in situ polymerization self-assembly of 3,4-ethylenedioxythiophene (EDOT) on MXene-$Ti_3C_2T_x$ in an aqueous solution without any oxidant. Notably, the polymerized EDOT long-chains confined between the MXene-$Ti_3C_2T_x$ layers form an envelope of the conductive network in the MXene-$Ti_3C_2T_x$@EDOT hybrid structure. Thereafter, the proposed MXene-$Ti_3C_2T_x$@EDOT hybrid is electrophoretically deposited on laser-induced graphene (LIG) leading to LIG/MXene-$Ti_3C_2T_x$@EDOT composite, exploiting the electrical and mechanical properties. The electronegative property of MXene-$Ti_3C_2T_x$ allows the assembled composite material to have easy electrophoretic deposition (EPD) on the conductive substrate connected to the positive electrode. Moreover, the EPD mechanism mitigates the limitations of uneven thickness of the conductive film caused by drop-casting or spin coating of hydrophilic materials on the hydrophobic substrate. To realize the multifunctional sensing ability of the device, various patterns of the sensing layers are replicated into ultrathin (143 µm) and highly resilient polystyrene-*block*-poly(ethylene-*ran*-butylene)-*block*-polystyrene (SEBS) and packaged into a layer-by-layer assembly. Finally, to demonstrate the suitability of LIG/MXene-$Ti_3C_2T_x$@EDOT composite material for multifunctional sensors, we monitor subtle to large human-body induced deformations, including temperature characterizations and ECG monitoring. The composite material exhibits high strain sensitivity (2075; > 22% strain) a good TCR (0.52% K^{-1}) and low skin-electrode impedance (51.08 kΩ at 10 Hz) making it suitable for strain, temperature, and biopotential measurements, respectively. More impressively, the method is scalable, facile, and cost-effective for the fabrication of high-performance multifunctional sensors because of the single-step EPD without needing any oxidant and easy transfer of functional materials into an ultrathin stretchable substrate and their layer-by-layer packaging.

RESULTS AND DISCUSSION

Multifunctional sensor fabrication

The fabrication of the multifunctional sensor involves laser engraving of the patterns, the EPD mechanism of MXene-$Ti_3C_2T_x$@EDOT on LIG, transferring the patterns into SEBS substrate, and encapsulation by SEBS (Fig. 1a). Briefly, MXene-$Ti_3C_2T_x$ flakes are obtained by the selective etching of an Al layer from the MAX phase-Ti_3AlC_2 (see Methods for detail). As a supporting layer, LIG was obtained by laser engraving of PI (Kapton) film using a 10.6 µm CO_2 microlaser at a speed of 60 mm/s and laser power of 19%. After that, as prepared MXene-$Ti_3C_2T_x$@EDOT composite material was subjected to an EPD mechanism. During this stage, negatively charged MXene-$Ti_3C_2T_x$ @EDOT composite has been successfully self-assembled, which allows the assembled material to be easily deposited on the conductive LIG substrate connected to the positive electrode. To achieve high stretchability, elastic recovery, and high cycling stability, we transferred LIG/MXene-$Ti_3C_2T_x$ @EDOT composite patterns into the SEBS substrate. Based on the target applications and encapsulation requirements, the sensing layers are either encapsulated or exposed outside by arranging in a layer-by-layer assembly (Fig. 1b). A key constraint of previous multifunctional devices is the challenge to efficiently integrate individual sensors into a single substrate due to complex fabrication. Here, such integration was achieved by hot pressing of stacked individual sensors. In addition, the strain-invariant design strategy for the temperature sensor and ECG electrode was adopted in such a way that meandering structures are in the transverse direction to that of the tensile strain direction. The detailed procedure for the fabrication of the LIG/MXene-$Ti_3C_2T_x$ @EDOT-based multifunctional sensor is described in the Methods section. Figure 1c shows the photograph of the replication of LIG patterns into SEBS. Interestingly, the functional material (i.e., LIG/MXene-$Ti_3C_2T_x$@EDOT) resulting from the EPD mechanism has good adhesion with LIG and with underlying SEBS substrate (Supplementary Fig. 1). After stacking individual sensors in a layer-by-layer fashion, the final sensor assembly is shown in Fig. 1d.

To meet the requirement of flexible sensing material, we employed the strategy of combining MXene-$Ti_3C_2T_x$ with organic molecules or polymer, which is one of the best alternatives to enhance the mechanical properties and biocompatibility. We selected EDOT as the candidate monomer to investigate the MXene-$Ti_3C_2T_x$ promoted in situ polymerization without the need for any oxidant. Here, MXene-$Ti_3C_2T_x$ layers serve as a substrate for the synthesis and alignment of the EDOT chains. As MXene-$Ti_3C_2T_x$ flakes are a negatively charged material with the active electrophilic surface due to the presence of −OH, −F, and −O functional groups, EDOT chains are densely grown on all MXene-$Ti_3C_2T_x$

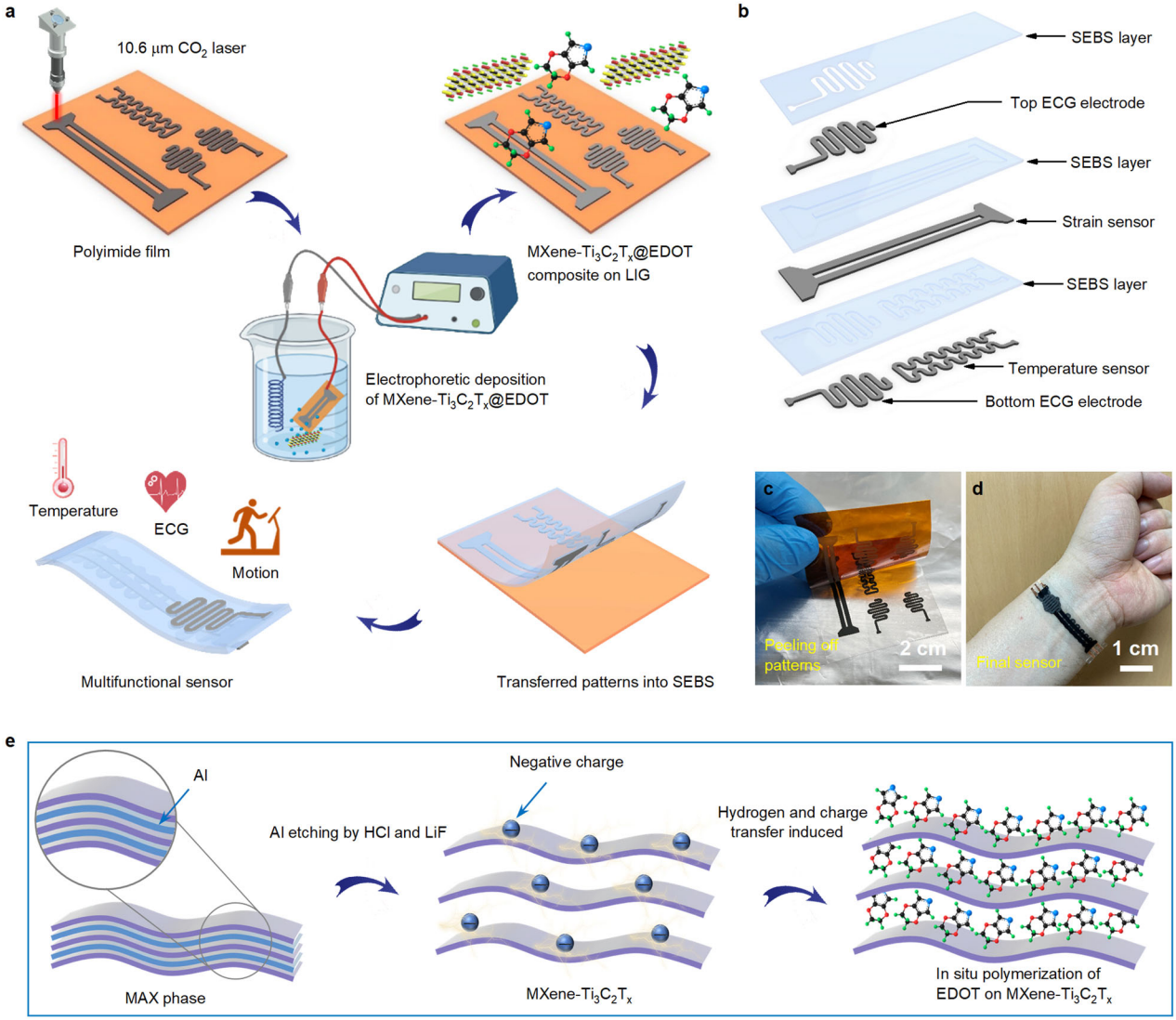

Fig. 1 Illustration of fabrication of multifunctional sensors. (**a**) Schematics of the fabrication of the LIG/MXene-$Ti_3C_2T_x$@EDOT-based multifunctional sensors. (**b**) Layered view of the sensors. Photograph of the (**c**) transferring of LIG/MXene-$Ti_3C_2T_x$@EDOT patterns into SEBS and (**d**) final sensor. (**e**) Mechanism of in-situ polymerization of EDOT on MXene. (Photo credit: Shipeng Zhang, Kwangwoon University.).

surfaces because of self-alignment induced in-situ polymerization mechanism (Fig. 1e). The self-alignment-induced in-situ polymerization mechanism is greatly assisted by charge transfer and hydrogen bonding[38,39]. In the MXene-$Ti_3C_2T_x$@EDOT hybrid, the hydrogen bonding originates from the C–H group of the EDOT and terminating −O or −F present on the MXene-$Ti_3C_2T_x$ surface, similar to the mechanism achieved for polypyrrole and polyaniline on MXene-$Ti_3C_2T_x$ nanosheets[39,40]. In addition, hydrogen bonding between the anion and the surface of the electrode promotes the self-alignment of EDOT oligomers[41]. As such, the EPD mechanism of the MXene-$Ti_3C_2T_x$@EDOT hybrid on LIG was successfully achieved in an aqueous solution. The functional groups (−NH_2 −COOH, −OH) present in the LIG are covalently bonded with MXene-$Ti_3C_2T_x$ possessing Ti–OH(F) functional groups (Fig. 2a). Besides, the LIG acts as a supporting layer for the functionalization of both covalent and noncovalent functionalization.

Analytical characterization

The usefulness of the EPD mechanism was further confirmed by field emission scanning electron microscopy (FESEM). As seen from the FESEM image of Fig. 2b, MXene-$Ti_3C_2T_x$@EDOT deposited on the pristine LIG substrate (Supplementary Fig. 2a) by direct drop-casting, it is clear that the material cannot be uniformly deposited on the LIG surface. The MXene-$Ti_3C_2T_x$ prepared by etching and exfoliation of MAX phase $Ti_3C_2T_x$ using HCl and LiF results in multilayered nanosheets-like structure as shown in FESEM image of Supplementary Fig. 2b. There is a severe aggregation phenomenon, which significantly affects the electrical performance of the sensor[14]. However, in the self-assembled EPD mechanism, the MXene-$Ti_3C_2T_x$ @EDOT composite was uniformly deposited on the LIG substrate (Fig. 2c). The inset shows a high-resolution FESEM image of the MXene-$Ti_3C_2T_x$ @EDOT composite nanosheets. To confirm the uniformity of the MXene-$Ti_3C_2T_x$ @EDOT deposited by the EPD mechanism, we have taken the FESEM images of the cross-section (Supplementary Fig. 2c-d). An average thickness of the LIG/MXene-$Ti_3C_2T_x$@EDOT calculated from six different locations was found to be approximately 29.37 μm with a mean error of 989 nm. Furthermore, the comparison between surface profiles of drop-casting and EPD mechanisms has been investigated by atomic force microscopy (AFM). As seen from the AFM images of Supplementary Fig. 3a-b, direct drop-casting of MXene-$Ti_3C_2T_x$@EDOT leads to a non-uniform surface profile attributed to the aggregation of

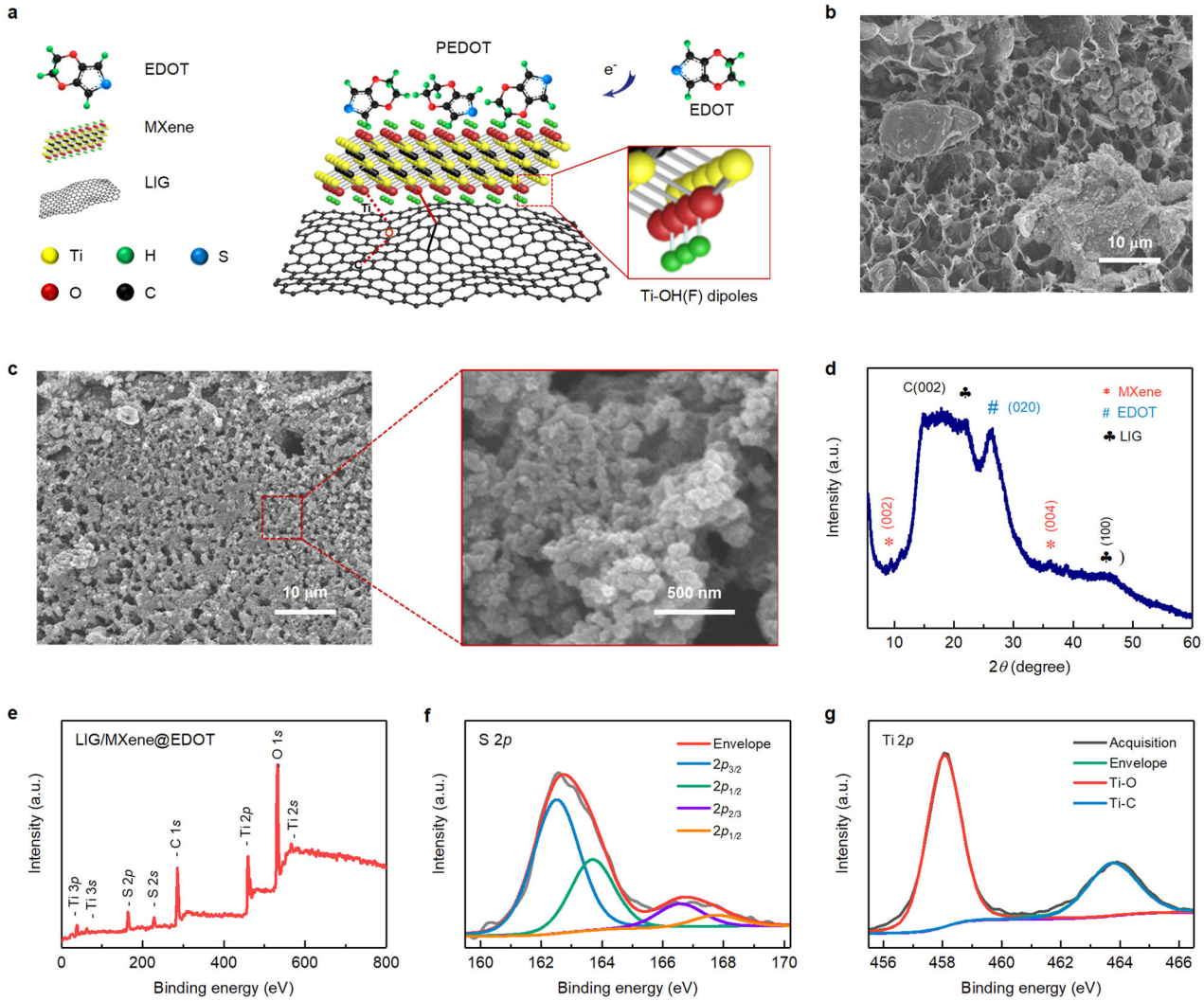

Fig. 2 Physical characterization of the composite material. (**a**) 3D chemical and physical crosslinking of the LIG, MXene-$Ti_3C_2T_x$, and EDOT. (**b**) FESEM image of drop-casted MXene-$Ti_3C_2T_x$@EDOT on LIG. (**c**) FESEM image of MXene-$Ti_3C_2T_x$@EDOT on LIG after electrophoretic deposition (high-resolution FESEM in inset). (**d**) XRD and (**e**) XPS survey spectrums of LIG/MXene-$Ti_3C_2T_x$@EDOT composite. XPS spectrum of (**f**) S 2*p* and (G) Ti 2*p* region.

MXene-$Ti_3C_2T_x$@EDOT into LIG. However, MXene-$Ti_3C_2T_x$@EDOT deposited from the EPD mechanism has a smooth and uniform surface. It confirms that EPD can effectively enhance the uniform material deposition, leading to a smooth thickness of the sensor. Besides, the long-chain structure of EDOTs is knitted with the loosely coupled MXene-$Ti_3C_2T_x$ nanosheets into a good anchoring, thereby significantly improving the orderliness of the layer structures and electronic pathways. Therefore, this type of structure endows the high elasticity of the MXene-$Ti_3C_2T_x$@EDOT polymeric film. The chemical structure of the MXene-$Ti_3C_2T_x$@EDOT composite material was investigated by X-ray diffraction (XRD) and X-ray photoelectron spectroscopy (XPS) analysis. Figure 2d shows the XRD patterns of the LIG/MXene-$Ti_3C_2T_x$@EDOT films obtained through the EPD mechanism. The MXene-$Ti_3C_2T_x$@EDOT composite shows primary diffraction peaks at 10.0° and 38.0° assigned to the characteristic (002) and (004) planes, respectively, which indicates the presence of MXene[42]. An additional peak at 27.0° is assigned to the characteristic (020) plane, indicating the presence of EDOT[43]. The XPS spectrum (Fig. 2e) was used to characterize the surface chemical environment of the synthesized LIG/MXene-$Ti_3C_2T_x$@EDOT composite. In the XPS survey region (0 – 800 eV), peaks from the C, Ti, S 2*p*, and O elements are well distinguishable. Figure 2 (f and g) show the high-resolution XPS spectra of the S 2*p* and Ti 2*p* regions, respectively. The S 2*p* spectrum reveals the presence of four separate peaks, which are related to S $2p_{3/2}$ (162.2 eV), S $2p_{1/2}$ (163.9 eV), S $2p_{2/3}$ (166.5 eV), and S $2p_{1/2}$ (167.9 eV)[44,45]. The Ti 2*p* spectrum (Fig. 2g) reveals the presence of two separate peaks, which are related to Ti−O (458.2 eV) and Ti−C (463.9 eV). These results are in accordance with those of the previous reports[46,47]. The presence of the S 2*p* and Ti 2*p* peaks indicates a successful deposition of MXene-$Ti_3C_2T_x$@EDOT on LIG. Furthermore, the elemental composition of the synthesized LIG/MXene-$Ti_3C_2T_x$@EDOT was carefully investigated through energy dispersive spectrometer (EDS) mapping (Supplementary Fig. 4). The atomic percentages of C, O, S, and Ti were mapped as 29.54, 41.79, 20.40, and 8.27%, respectively, well agreeing with the XPS results.

Electromechanical characterization

The schematic illustration of the patterned LIG/MXene-$Ti_3C_2T_x$@EDOT-based strain sensor before stretching and under stretching conditions is shown in Fig. 3a and photographed images are depicted in Supplementary Fig. 5a. The inset shows the schematic

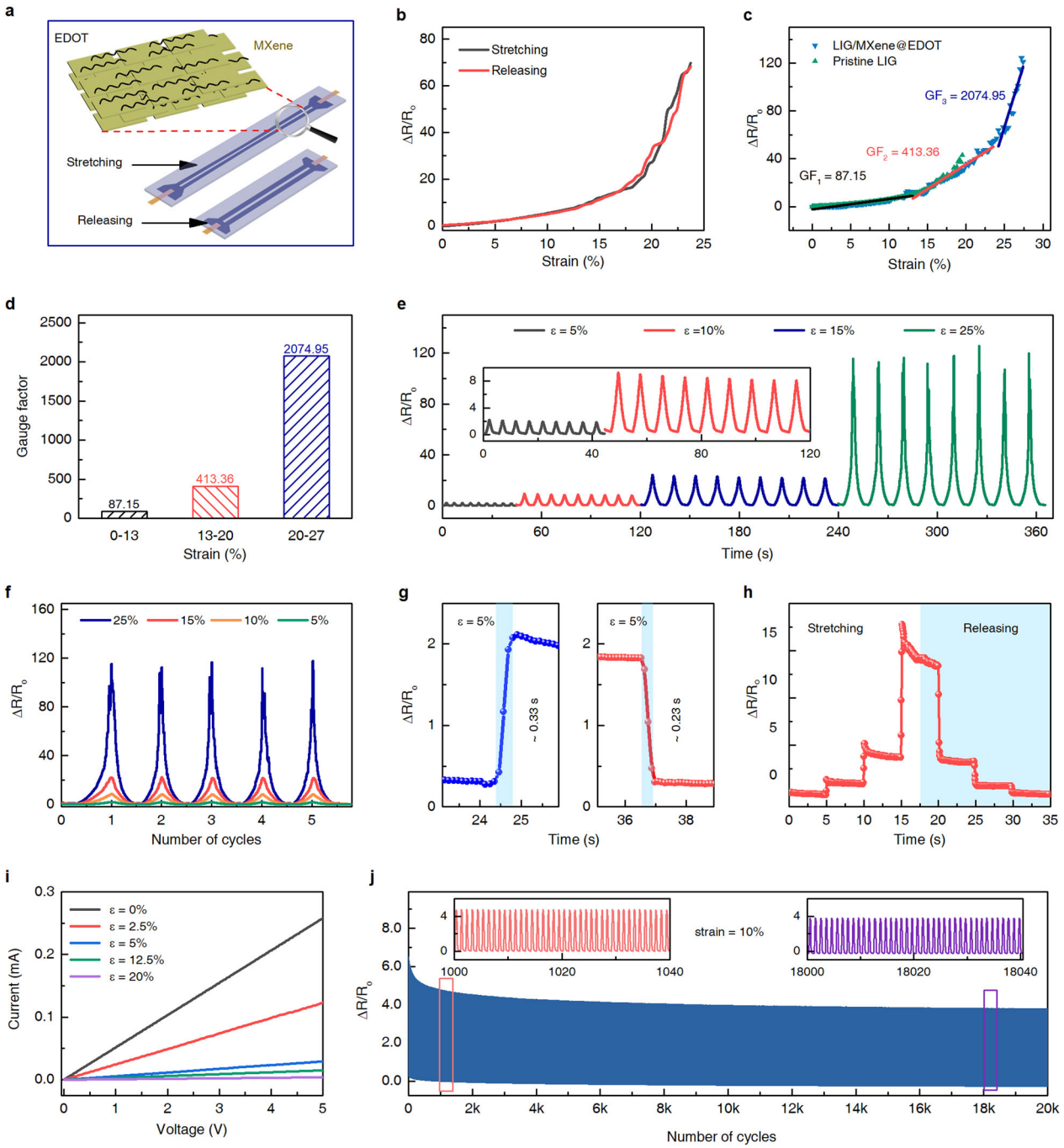

Fig. 3 Electromechanical characterization of strain sensor. (**a**) Schematics showing the mechanism of crack propagation during stretching. (**b**) Measurement of electrical hysteresis during stretching (black line) and releasing (red line) up to a safer limit of 23%. (**c**) Change in resistance vs. strain depicting strain sensitivity. (**d**) Statistical GFs at different strains. (**e**) Time-dependent and (**f**) corresponding cyclic response of the strain sensor for consecutive cycles of strains from 5 to 25%. (**g**) Calculation of dynamic response and relaxation time. (**h**) Sequential stretch and release process depicting reversibility of resistance response. (**i**) Verification of Ohm's law showing the piezoresistive nature of the sensor. (**j**) Durability test of the sensor measured over 20,000 cycles.

illustration of the alignment of MXene-$Ti_3C_2T_x$ flakes and EDOT chains on the LIG substrate. The long-chain structure of EDOT is knitted to the loosely coupled MXene nanosheets forming a good anchoring for electronic pathways. The change in resistance (ΔR) originates from any individual or combined effect of the following mechanisms: structural geometry change, tunneling resistance, resistivity change, and composite microcrack propagation[35]. The stress-strain profile of the functional material with and without EDOT has also been examined. The material without EDOT (Supplementary Fig. 5b) offers larger cracks, leading to a higher change in resistance at the same level of strain but the resistance response is not uniform and suffers from perfect recovery in electrical resistance. However, the relative change in resistance resulting from strain loading and release demonstrates that the resistance for strain release follows the same path as traced during stretching (Fig. 3b), thereby suggesting negligible sensor

hysteresis. The figure of merit to compare the strain sensitivity (i.e., GF), the ratio of relative change in resistance to that in strain is defined by the following formula

$$GF = \frac{\delta(R - R_o)/R_o}{\delta\varepsilon} \quad (1)$$

where $\varepsilon = \Delta L/L_o$ is the normalized change in length (or applied strain). The entire reversible region was categorized into three linear sensitivity regions: 0–13, 13–22.5, and >22.5 with GFs of approximately 87, 413, and 2,075, respectively (Fig. 3c). In a low-strain regime, smooth response and high mathematical value of GF resulted from linear crack formations and the structural geometry changes, respectively[14,20,35]. The LIG/MXene-$Ti_3C_2T_x$@EDOT conductive porous network ruptured slightly at moderate strains, thereby impeding the conducting pathways. For moderate and high tensile strains, a distinct shift in resistance occurred as a consequence and higher GF mathematical values were obtained. However, high mathematical values of GF are still possible for strain higher than 28%, but high strain often leads to an irreversible resistance response[35]. To achieve high GF, the sensor should undergo significant structural changes with minimal deformation, thereby changing the conductive networks significantly and producing resistance signals with strain changes. Furthermore, obtaining a wide sensing range requires the sensor to be subjected to large deformations while maintaining the connectivity of the material[48,49]. It should be noted is that complete disconnection of the electrical pathways leads to a high mathematical value of GF but it does not guarantee the reversibility and precision of the response. The resiliency of the substrate materials merely determines the reversibility of the response. Therefore, we exploited a highly stretchable and resilient polymer, SEBS, as a substrate for our sensor. We also fabricated a sensor from pristine LIG to compare the performance of LIG/MXene-$Ti_3C_2T_x$@EDOT-based sensor by following the same process as used for LIG/MXene-$Ti_3C_2T_x$@EDOT. Notably, both the sensors have identical GFs for strain lower than 20%. However, when the applied strain exceeds 20%, the electrical connection was completely lost on pristine LIG. This is because LIG nanoflakes only cannot maintain electrical conductivity over a large strain. The statistical value of GFs of the LIG/MXene-$Ti_3C_2T_x$@EDOT strain sensor is shown in Fig. 3d. Furthermore, the relative change in resistance of the LIG/MXene-$Ti_3C_2T_x$@EDOT-based strain sensor was subsequently examined for strain values ranging from 5 to 25%, and the results are depicted in Fig. 3e. The inset shows the enlarged view of the response low strains. Similarly, the cyclic response was also assessed by applying different strains ranging from 5 to 25% while continuously measuring the resistance. The sensor response increased monotonically with strain and recovered reversibly with strain release (Fig. 3f).

In addition, the dynamic response and relaxation time of the sensor were measured at 5% strain. For the time when the strain was applied, the response of the sensor was consistently sustained and recovered to its original value upon release. The duration of dynamic response (and relaxation) depends on how quickly the sensor responds to the loading strain (and unloading). The time interval between the adjacent level change was reported as 0.33 s (during stretching) and 0.23 s (during release), with a maximum possible stretching speed of 600 mm/s, thereby indicating faster recovery upon release (Fig. 3g). The relaxation time is significantly improved because of the incorporation of EDOT chains, which worked as a bridge to bind the MXene-$Ti_3C_2T_x$ flakes to recover electrical connection upon strain release. To access the reversibility of the sensor, the staircase response of the sensor was investigated by sequentially stretching by 2 mm (5% strain) and maintaining it for 5 s. When the strain reached 20%, it was released with the same step size as applied during the stretching. The consistency of the staircase stretch release path also indicates the good reversibility of the sensor (Fig. 3h). The piezoresistive nature of the LIG/MXene-$Ti_3C_2T_x$@EDOT-based sensor was confirmed by examining current-voltage (*I-V*) characteristics at various strains (0 to 20%). With a bias potential of 1 V, the current increases monotonically, thereby obeying the linear relation of Ohm's law (Fig. 3i). Meanwhile, it is observed that the slope of the *I-V* curve decreases with increasing strains because of the relative increase in resistance, thereby confirming the piezoresistive existence of the LIG/MXene-$Ti_3C_2T_x$@EDOT-based strain sensor. For strains higher than 20%, the slope of the *I-V* curve was almost flat, thereby suggesting infinite resistance between the conductive pathways. Furthermore, as prepared LIG/MXene-$Ti_3C_2T_x$@EDOT strain sensor exhibited good stability over 20,000 cycles as shown in Fig. 3j. The long-term durability of the sensor is due to the synergistic effect of increased interlayer spacing between MXene-$Ti_3C_2T_x$ layers. However, a slight overshoot in the incipient cycles of the durability test was caused by the viscoelastic nature of the polymer, producing creep behavior. The inset shows a more illustrative form of the few representative cycles (40 cycles) of the durability test at the beginning (100 cycles) and ending (18,000 cycles). A representative test was also conducted for a comparatively lower cyclic strain of 4% for 1,000 cycles (Supplementary Fig. 5c). Overall, uniform and reversible resistance was resulted due to microcracks propagation between the MXene-$Ti_3C_2T_x$ flakes during the stretching and resulted in a large variation in resistance (Supplementary Fig. 5d). While EDOT acts as bridging materials between MXene-$Ti_3C_2T_x$ nanoflakes and preserved electrical conductivity over the large strain. Furthermore, the formation of microcracks and their reconnection were also examined by FESEM (Supplementary Fig. 6). After releasing the strain, the cracks are reconnected reversibly to regain the electrical resistance due to the presence of EDOT and SEBS as bridging material and resilient substrate, respectively. The synergistic effect of EDOT and MXene-$Ti_3C_2T_x$ nanosheets was responsible for the outstanding sensing performance. To the best of our knowledge, the sensitivity and reliability of the LIG/MXene-$Ti_3C_2T_x$@EDOT strain sensor are significantly better than those of the state-of-the-art strain sensors, as presented in Table 1.

Human motion detection

The high GF of our sensor manifests its ability to successfully measure the full range of human body motions from subtle deformations to large bending. As depicted in photographed images of Fig. 4a, the sensor was mounted on different locations of the human body to measure vocal vibration, wrist pulse, twitching motion, and finger bending. As a demonstration of voice sensing, the sensor was attached above the larynx to examine the reaction of the epidermis motion caused by the vibration of the vocal cord. A volunteer was asked to pronounce various phrases, such as 'nice to meet you' and 'happy birthday' (Fig. 4b). Notably, the sensor showed similar responses in each period for the cyclic pronunciation of each phrase, while the patterns varied from each other depending on the syllables. The repeatability of the detection was good in each successive testing. The detection of quick and delicate phonation means the sensor could distinguish numerous syllables in simple words, thereby indicating a possible scope in voice monitoring. Similarly, we applied the sensor for human wrist pulse measurement to demonstrate the capability of the sensor for subtle strain detection. The sensor was placed by wrapping an adhesive tape over the radial artery of an adult male and a corresponding resistance response was recorded (Fig. 4c). The arterial pulse rate, calculated from two successive systolic peaks, was found to be 68 beats per minute with a time interval of approximately 0.84 s. The enlarged view of one pulse period obtained from the time-averaged signal of eight periods clearly shows that the presence of the percussion wave (P-wave) and diastolic wave (D-wave), which fortifies the usefulness of the senor for arterial wrist pulse

Table 1. Comparison of the performance of the recent piezoresistive strain sensors and their sensing materials.

refs.	sensing materials	GF/strain ranges [%]			stability
		low	medium	high	
[3]	‡LSG/Ecoflex	11 (0–2.5)	92 (2.5-4.5)	673 (4.5–5)	1000
[9]	AgNWs on dragon skin	24.6 (0–130)	–	81 (130–150)	10,000
[14]	MXene /CNT	64.6 (0–30)	–	772.6 (40–70)	5000
[17]	Graphene/Ecoflex	0.6 (<5)	–	17.4 (5<ε<200)	–
[22]	MXene /PDMS	178 (0–5)	505.1 (5-35)	1176 (35–53)	5000
[37]	LIG/PI	1.16 (10)	–	–	–
[55]	MoS_2/LIG on PDMS	236 (0–16.7)	–	1242 (<25)	12,000
[56]	AuNWs/Latex	9.9 (0–5)	–	6.9 (5–50)	>5000
This work	MXene@EDOT/ §LIG on SEBS	87 (1–13)	413 (13–22.5)	2075 (>22.5)	20,000

‡Laser-scribed graphene; §Laser-induced graphene.

measurement (Fig. 4d). These are significant clinical indicators for the diagnosis of arterial stiffness and cardiovascular disease. The sensor is highly stretchable; thus, it can easily be attached to a body arthrosis surface to monitor human-body-induced large deformations as well. Different body movements can be tracked by mounting the sensor on a knuckle and arm muscle. Furthermore, we attached the sensor over the arm muscle of the forearm to allow the detection of arm muscle motions. The forearm muscle contraction and relaxation were accurately measured for five consecutive cycles (Fig. 4e). Similarly, we attached the sensor over the second knuckle (proximal interphalangeal joint) of the forefinger to facilitate finger bending detection. The bending of the finger at various bending angles (0-60°) was precisely tracked by monitoring the relative change in resistance response (Fig. 4f). For a large bending angle of 60°, the relative change in resistance response exhibited higher values because of overstretching of the sensor. Notably, the sensor regains its baseline resistance quickly. We also developed and integrated a flexible low-power RF energy harvesting battery-free near field communication (NFC) wireless patch system to transmit the strain data to a smartphone wirelessly (Supplementary Fig. 7a). The flexible antenna and circuit were soldered using a low-temperature solder paste with all the components surface-mounted (SMD) (Supplementary Fig. 7b). The electronics design, measurement strategy, and the complete system are shown in Supplementary Fig. 7c. Here, LIG/MXene-$Ti_3C_2T_x$@EDOT strain sensor was integrated with a flexible, battery-free NFC wireless patch system, and output galvanic strain response at different finger bending angles was measured and received wirelessly (Supplementary Fig. 7d and movie 1).

Temperature characterization

The stretchable temperature sensors should elicit accurate and stable performance even under stretching conditions. However, most of the flexible sensors undergo deformations on the sensing area and results in unstable output performances. Therefore, we have deliberately designed the strain-insensitive serpentine patterns at the bottom layer and were not fully encapsulated by the polymeric substrate layer. Although the strain-induced does not affect the temperature sensing layer, such as Kirigami structures[13], the sensor mounted on strain-insensitive body locations (Fig. 5a) can deliver more accurate and precise results. The temperature responsivity of LIG/MXene-$Ti_3C_2T_x$@EDOT composite material was first studied by elevating the temperature while recording resistances (Supplementary Fig. 8a). The resistances as a function of temperature were best fitted by non-linear exponential (Fig. 5b). The linear relationship between *ln(R)* and $1/T$ can be expected from an Arrhenius-type equation

$$\ln(R) = \ln(R_\infty) + \frac{E_a}{2k_BT} = \ln(R_\infty) + \frac{B}{T} \quad (2)$$

where $B = E_a/2K_BT$ is the thermal index, k_B is the Boltzmann constant, R is the instantaneous resistance at a particular temperature T, and R_∞ is the resistance at infinite temperature. From the variation of *ln(R) vs. 1/T*, the values for B were calculated (Supplementary Fig. 8b-c). Based on the value of B, the thermal activation energy E_a was calculated to be 89.2 meV. From Eq. (2), we can correlate TCR to thermal index as

$$\frac{1}{R}\frac{dR}{dT} = -\frac{E_a}{2k_BT^2} = -\frac{B}{T^2} \quad (3)$$

This is an expression for TCR at a particular temperature T. However, for performance evaluation of our LIG/MXene-$Ti_3C_2T_x$@EDOT composite material, the temperature sensitivity, i.e., TCR was calculated from the slope of the curve by using

$$TCR = \frac{dR}{R_o dT} \quad (4)$$

where the factor dR/R_o is the relative change in resistance, while ΔT is the temperature deviation measured in K with reference temperature set to 26 °C. The resistance significantly changes with temperature, exhibiting negative temperature dependency (Fig. 5c). As obtained from the linear curve fitting, our material exhibited an exceptional TCR of 0.52% K^{-1}, which is superior compared to state-of-the-art thermistors[10,11,13,18,35] (Supplementary Table 1). The response of the temperature sensor at different temperatures measured at the physiological temperature range also supports the negative temperature coefficient behavior of LIG/MXene-$Ti_3C_2T_x$@EDOT (Fig. 5d). Compared to inflexible substrates with a low coefficient of thermal expansion (CTE), such as glass, stretchable materials with high CTE expands faster resulting increase in resistance of the material because of the inter-particle distance mechanism[11,35]. However, in our sensor, as LIG/MXene-$Ti_3C_2T_x$@EDOT is not fully encapsulated; the thermal expansion of the underlying SEBS substrate material is not dominant. The temperature-dependent electrical behaviors of LIG and charge carrier generation of MXene-$Ti_3C_2T_x$@EDOT at elevated temperatures enhance the charge transport behaviors and hence the conductivity of the composite material increases. Furthermore, the temperature-discrimination capacity of the proposed material was also measured by the cyclic test of elevating the temperature to 45 °C and cooling it down to 26 °C. The resistance values under each temperature show negligible deviation, implying stability and repeatability in response (Fig. 5e). The negligible deviation in

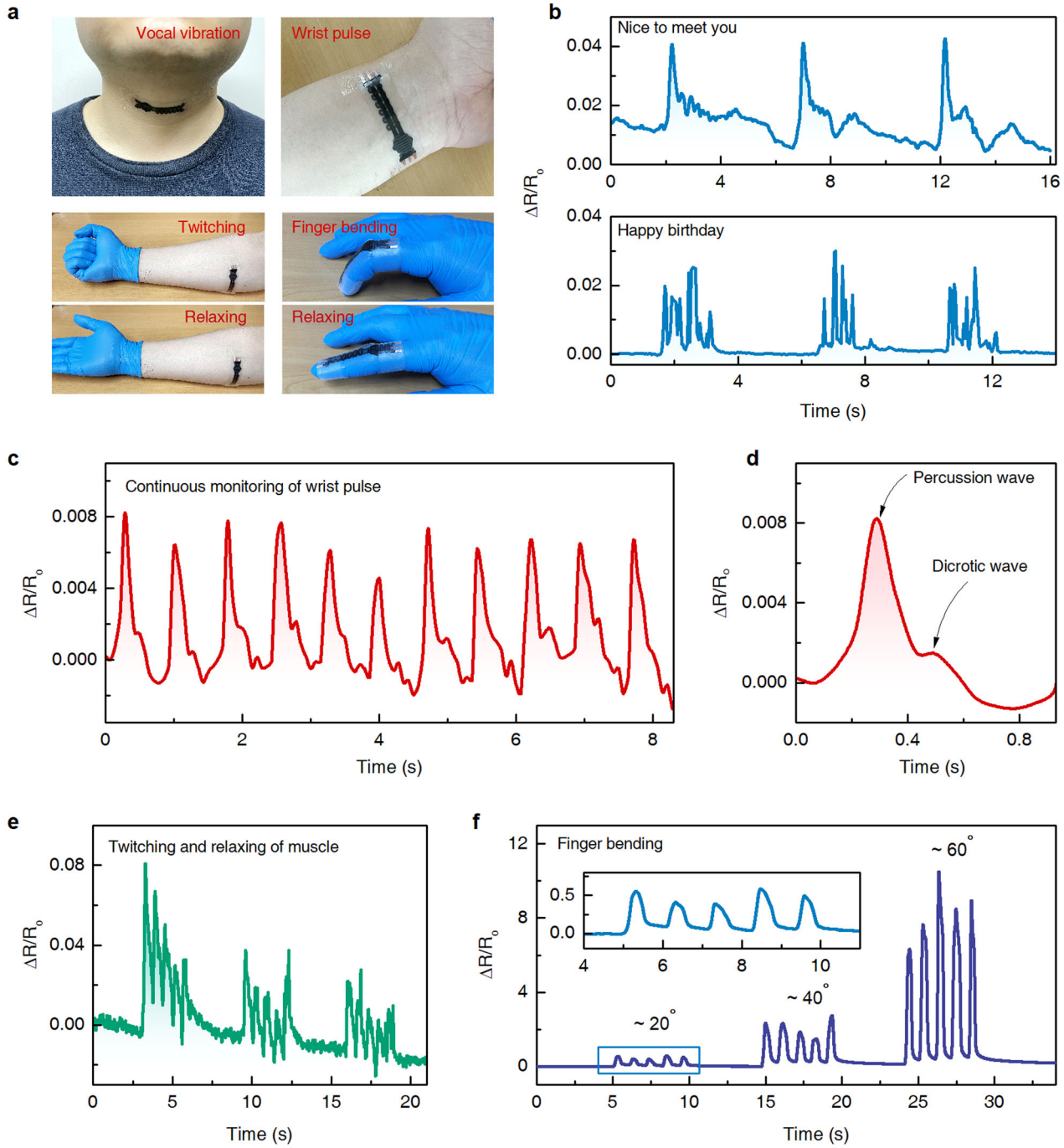

Fig. 4 Measurements of the human body induced deformations. (**a**) Photographs showing different locations to measure subtle to large human body-induced deformations. (**b**) Application of sensor as an artificial throat depicting the response for pronunciation of 'happy birthday' (top) and 'nice to meet you' (bottom). (**c**) Real-time resistance response of the sensor for wrist pulse and (**d**) time-averaged eight pulse periods containing P-wave and D-wave. (**e**) Response of the sensor for muscle twitching. (**f**) The ability of the sensor for the human body induced large motion detection as finger bending and relaxing. (Photo credit: Ashok Chhetry, Kwangwoon University.).

the relative change in resistance of 0.011 and 0.013 at an upper and lower temperature, respectively confirm the viability of the LIG/MXene-$Ti_3C_2T_x$@EDOT composite material for the stretchable strain-insensitive temperature sensor.

Physiological signal measurements

Human epidermal biopotentials, such as ECG are significant for the diagnosis and treatment of heart-related diseases. These biopotentials can be transduced by electrically interfacing with the skin via epidermal electrodes. The suitability of the LIG/MXene-$Ti_3C_2T_x$@EDOT composite material for ECG measurement was confirmed by evaluating epidermal biopotentials. To measure ECG signals, the sensor was placed on the volunteer's left wrist (LA) ensuring the bottom ECG electrode was contacted to the skin and the top electrode (RA) was touched by the right hand's finger (Fig. 5f). Owing to the high conductivity of LIG/MXene-$Ti_3C_2T_x$@EDOT (LME) electrode, impedance spectra as a function of frequencies were measured in the frequency range from 4 Hz to

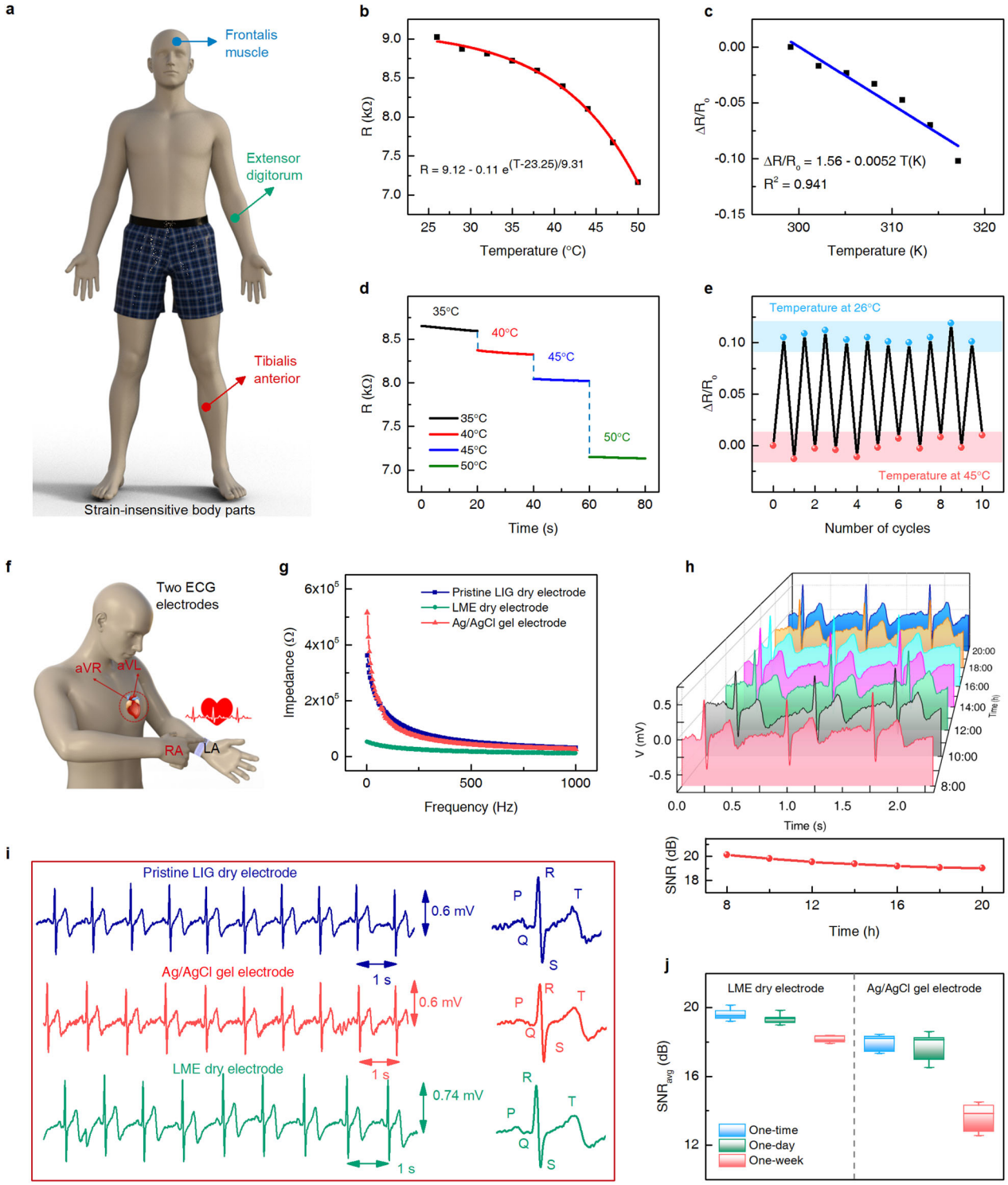

Fig. 5 Physiological signals measurement. (**a**) Illustration of strain-insensitive body parts for temperature measurement. (**b**) Resistance response of LIG/MXene-$Ti_3C_2T_x$@EDOT composite as a function of temperature. (**c**) Calculation of thermal index as temperature sensitivity. (**d**) Response of the temperature sensor at physiological temperature range. (**e**) Temperature discrimination ability. (**f**) Illustration of ECG detection mechanism. (**g**) Comparison of contact impedance spectra as a function of frequency. (**h**) Long-term ECG monitoring (top) and their SNR measured for 12 h (bottom). (**i**) Long-term ECG monitoring for LIG, LIG/MXene-$Ti_3C_2T_x$@EDOT, and Ag/AgCl gel electrode. (**j**) Comparison of SNR of our sensor with Ag/AgCl gel electrode over one week.

1 kHz. For the skin-electrode impedance measurement, two identical LME electrodes were put on the skin at a distance of 3 cm apart and impedance spectra were measured. As evident from the equivalent circuit model of the dry electrode (Supplementary Fig. 9a), skin-electrode impedance decreases with increased frequency. The LME electrode exhibited a significantly lower skin-contact impedance of 51.08 kΩ at 10 Hz (Supplementary Fig. 9b), lower than that of the Ag/AgCl electrode (417.86 kΩ).

The stable and low contact impedance results in accurate ECG recording and better signal-to-noise ratio (SNR)[50,51]. Therefore, it is desirable to have a low contact impedance of the skin-electrode interface for improved signal quality.

Our LME electrode resulted in high-quality ECG signals with the characteristics of PQRST waveforms (Supplementary Fig. 9c and movie 2). Compared to the pristine LIG dry electrode and Ag/AgCl gel electrode, the LIG/MXene-$Ti_3C_2T_x$@EDOT composite-based (LME) electrode has the highest QRS complex of 0.74 mV (Fig. 5i). The viability of the composite material for consistent and long-term signal monitoring was evaluated by measuring ECG every 2 h interval throughout 12 h (Fig. 5h, top). In addition, the SNR of the ECG signal was evaluated using

$$SNR(dB) = 10\log\frac{V_{rmsf}}{V_{noise}} \quad (5)$$

where the subscript *rmsf* and *noise* in potential (*V*) refers to the root-mean-square (RMS) value of the filtered and noisy signal, respectively. The SNR value acquired by the LME electrode is approximately 20.14 dB initially and changes to 19.04 dB after 8 h of measurement time (Fig. 5h, bottom). The comparison of the average value of the SNR produced by our LME electrode and that of a gold standard measured up to one week is presented in Supplementary Fig. 9d. There is no significant signal deterioration even up to one week, implying the suitability of LIG/MXene-$Ti_3C_2T_x$@EDOT composite for long-term ECG monitoring. The signal quality is much better than the Ag/AgCl and other dry electrodes in the literature (Supplementary Table 2)[1,26,27,50]. The ECG signal can sufficiently provide information about cardiovascular disease-related abnormalities, such as arrhythmia, myocardial infarction, hypertrophy, and ischemia[52,53]. Furthermore, the skin compatibility of the LME dry and that of Ag/AgCl gel electrodes were investigated by attaching respective electrodes to the forearm continuously for 24 h. The LME electrodes hardly irritate the skin, no skin irritation was observed even after prolonged use of 24 h (Supplementary Fig. 9e). Furthermore, the multifunctional ability of the proposed sensor was investigated by simultaneous detection of subtle strain, temperature, and ECG monitoring. With the loading of the sensor to the wrist (say left arm), we can immediately measure the wrist pulse induced from the arterial vibration (Fig. 6a). The temperature sensors slowly respond to skin temperature (~36.6 °C) without any noticeable artifacts (Fig. 6b). The ECG signal was obtained immediately after touching the upper electrode by the right-hand finger (Fig. 6c). A slight delay in the output ECG signal is seen because of the time lag while touching the ECG electrode by the right-hand finger.

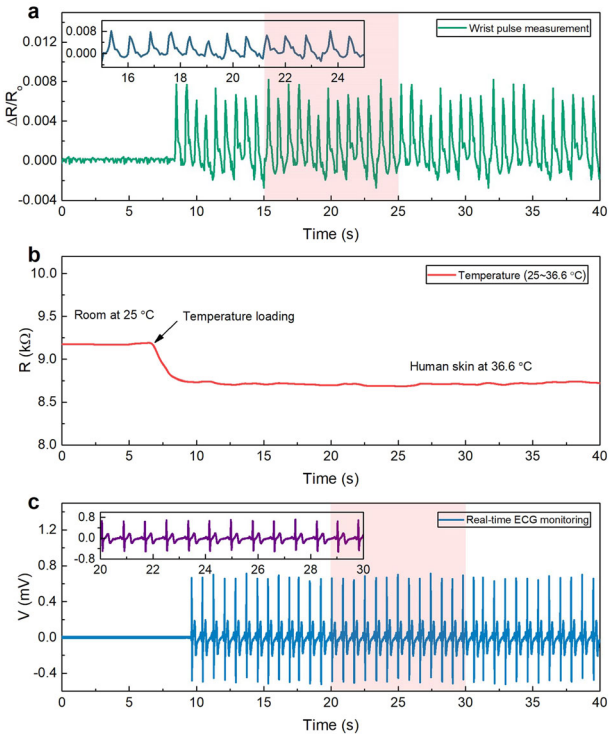

Fig. 6 Real-time detection. (**a**) subtle strain (i. e., wrist pulse), (**b**) skin temperature, and (**c**) ECG to validate the multifunctional ability of the proposed sensor. The sensor responds to the human wrist pulse and body temperature immediately after affixing it to the human wrist and later responds to ECG when touched by the right-hand finger.

DISCUSSION

In summary, this study demonstrates the fabrication of a highly sensitive, ultrathin, and reliable multifunctional sensor using the 3D envelope structure of the LIG/MXene-$Ti_3C_2T_x$@EDOT composite material in ultrathin stretchable SEBS substrate. As a proof of concept, we successfully demonstrated the integration of strain, temperature, and ECG sensors for simultaneous measurement of each stimulus. The capabilities mainly rely on three main advances over previous technologies: (i) integration of multiple sensors into an ultrathin and stretchable substrate in layer-bay-layer assembly, which is rarely possible in ordinary stretchable polymeric substrates, such as polydimethylsiloxane (PDMS), Ecoflex, and others, (ii) a design strategy for a multifunctional sensor to meet the requirements of enhancement of sensing parameters, and (iii) a piezoresistive composite material that is suitable for strain, temperature, and ECG measurements. The LIG/MXene-$Ti_3C_2T_x$@EDOT sensing layer was constructed using in situ polymerization self-assembly and EPD, thereby solving the uneven film thickness of the material deposition. In addition, the proposed LIG/MXene-$Ti_3C_2T_x$@EDOT composite exhibited high strain sensitivity, a wider working range, and long-term durability. The human-induced subtle deformations, such as arterial pulse and vibration of Adam's apples to larger body joint bending motions were successfully measured. The serpentine structure of the stretchable temperature sensor suppresses the effects of strain induced by body deformations. High TCR of the LIG/MXene-$Ti_3C_2T_x$@EDOT was attributed by charge carriers upon temperature loading and hopping transport. The material also has high conductivity, mechanical flexibility, and biocompatibility, possessing the suitability of epidermal biopotential measurement. The dry LME electrode exhibits low skin-electrode impedance and high-quality ECG signals. Furthermore, the concept provides an efficient strategy and cost-effective fabrication for the integration of multifunctional sensors into a stretchable platform. Overall, the versatile and scalable LIG/MXene-$Ti_3C_2T_x$@EDOT composite-based multifunctional sensor can provide a promising route to future wearable devices with artificial intelligence and comprehensive tracking ability of real-time physiological signals monitoring for e-skin and smart healthcare applications.

METHODS

Materials

The 3,4-ethylenedioxythiophene, polystyrene-*block*-poly(ethylene-*ran*-butylene)-*block*-polystyrene powder ($M_W \approx 118000$ with 21:9 mole ratio of styrene: rubber), toluene, and isopropyl alcohol were purchased from Sigma-Aldrich. MAX phase-Ti_3AlC_2 (particle sizes ≥ 38 μm) was purchased from Carbon-Ukraine Ltd. All commercially available chemical reagents were used without further purification.

Preparation of MXene@EDOT aqueous dispersion

MXene-$Ti_3C_2T_x$ nanosheets were prepared by etching and exfoliating the MAX phase $Ti_3C_2T_x$ using HCl and LiF as reported in our previous work[54]. The MXene- $Ti_3C_2T_x$@EDOT aqueous dispersion was prepared by dispersing MXene-$Ti_3C_2T_x$ (24 mg) EDOT (100 µL) in 20 mL deionized (DI) water. The suspension was magnetically stirred for 10 min and ultrasonicated for 1 h to achieve the MXene- $Ti_3C_2T_x$@EDOT aqueous dispersion.

Electrophoretic deposition of MXene@EDOT

The substrate material for MXene-$Ti_3C_2T_x$@EDOT was obtained by laser engraving of a commercial Kapton PI layer (125 µm) with a 10.6-µm CO_2 laser (Microlaser C40, Coryart, Korea) at a laser power of 7.6 W and a scan rate of 120 mm/s under ambient conditions. During the EPD process, the as-prepared 3D hierarchical porous network of conductive LIG was connected to the positive terminal of the supply (8 V DC) with the platinum electrode as the counter electrode for 10 min. In the MXene-$Ti_3C_2T_x$@EDOT solution, the electrodes were kept parallel at a distance of 1 cm from each other. A highly conductive LIG/MXene-$Ti_3C_2T_x$@EDOT composite was obtained by EPD of negatively charged MXene-$Ti_3C_2T_x$@EDOT hybrid on the LIG substrate, followed by drying at 40 °C for 3 h.

Fabrication of multifunctional sensor

The SEBS hybrid gel was prepared by dissolving SEBS triblock copolymer in toluene (150 g/L) and magnetically stirring until a transparent homogenous suspension was obtained. The conducting network patterns of LIG/MXene-$Ti_3C_2T_x$@EDOT for strain, temperature, and ECG were spin-coated (500 rpm, 30 s) by SEBS hybrid gel. The patterns were transferred into the SEBS via peel-off with the help of isopropyl alcohol after annealing for 8 h at 25 °C. The electrical connections were made by attaching Cu tapes with Ag paste. Finally, the patterns were arranged in a layer-by-layer assembly in such a way that the bottom ECG electrode and temperature sensor were facing down, strain sensor at the center, and top ECG electrode facing up, and heat pressed (QM100A Hotpress, Qmesys, Korea) at 90 °C/4 MPa for 10 min. Thanks to the ultrathin and resilient properties of the SEBS, without which the successful transferring of LIG/MXene-$Ti_3C_2T_x$@EDOT into an ultrathin substrate (~140 µm) and packaging of multiple sensors in layer-by-layer assembly just by heat pressing would not be possible.

Characterization and measurements

The as-fabricated LIG/MXene-$Ti_3C_2T_x$@EDOT electrodes were characterized by field emission scanning electron microscopy-FESEM (Quanta 250 FEG field emission environmental FESEM), Energy dispersive spectrometer (EDS) (JEOL JSM-6700F microscope), and X-ray photoelectron spectroscopy-XPS (ULVAC-PHI, Japan). The change in resistance of the LIG/MXene-$Ti_3C_2T_x$@EDOT composite material to strain, temperature, and frequency was measured with an LCR meter (IM 3536, Hioki). The same device was used to measure the impedance of the LME electrode while varying the input frequency from 4 Hz to 1 kHz. 3 M Tegaderm adhesive tape was used to attach the multifunctional sensor to different body parts. The fundamental characteristics of the temperature sensing were investigated by ramping up the temperature from the hot plate. Biopotential signals were acquired by mounting the bottom electrode (LA) on the wrist of the left arm with the top electrode (RA) touched by the right hand's forefinger. The ECG signals were obtained by connecting the LME electrode to the data acquisition and analysis system (MP160, BIOPAC System, Inc. USA). All post-processing was carried out using MATLAB software. The ECG signal was filtered using a sixth-order Butterworth low pass filter with a cutoff frequency of 50 Hz and SNR was calculated using Eq. (5). The optical images of crack propagation mechanisms under stretching conditions were taken by an AcquCAM Pro/U microscope with Olympus, UMPlan FI 20 × 0.25 BD lens.

Fabrication of NFC wireless system

Flexible antenna and circuit were fabricated by photolithography and wet etching of a copper foil-coated polyimide film. First, the photoresist (AZ GXR 601) was spin-coated on the commercial copper foil-coated polyamide film attached to the Si wafer. The wafer was cured at 90 °C for 10 min, and then a custom photomask was aligned using a mask aligner (MDA-400LJ) and exposed to UV light. The UV exposed patterns were etched by a copper etchant (10 min), followed by sequential cleaning by acetone, methanol, and DI water. Finally, the circuit was assembled using low-temperature solder paste with all the SMD components. The PDMS was coated and allowed to solidify at 50 °C for 2 h to encapsulate and protect the NFC electronics.

DATA AVAILABILITY

All relevant data that support the findings of this study are available from authors upon reasonable request.

Received: 25 August 2021; Accepted: 6 January 2022;
Published online: 08 February 2022

REFERENCES

1. Yamamoto, Y. et al. Printed multifunctional flexible device with an integrated motion sensor for health care monitoring. *Sci. Adv.* **2**, e1601473 (2016).
2. Yamamoto, Y. et al. Efficient Skin Temperature Sensor and Stable Gel-Less Sticky ECG Sensor for a Wearable Flexible Healthcare Patch. *Adv. Healthc. Mater.* **6**, 1–7 (2017).
3. Qiao, Y. et al. Multilayer Graphene Epidermal Electronic Skin. *ACS Nano* **12**, 8839–8846 (2018).
4. Ge, G. et al. Muscle-Inspired Self-Healing Hydrogels for Strain and Temperature Sensor. *ACS Nano* **14**, 218–228 (2020).
5. Yamada, T. et al. A stretchable carbon nanotube strain sensor for human-motion detection. *Nat. Nanotechnol.* **6**, 296–301 (2011).
6. Kim, T. et al. Heterogeneous sensing in a multifunctional soft sensor for human-robot interfaces. *Sci. Robot.* **5**, 1–14 (2020).
7. Nur, R. et al. A Highly Sensitive Capacitive-type Strain Sensor Using Wrinkled Ultrathin Gold Films. *Nano Lett.* **18**, 5610–5617 (2018).
8. Lee, J. et al. A stretchable strain sensor based on a metal nanoparticle thin film for human motion detection. *Nanoscale* **6**, 11932–11939 (2014).
9. Kim, K. H., Jang, N. S., Ha, S. H., Cho, J. H. & Kim, J. M. Highly Sensitive and Stretchable Resistive Strain Sensors Based on Microstructured Metal Nanowire/Elastomer Composite Films. *Small* **14**, 1–10 (2018).
10. Zou, Z. et al. Rehealable, fully recyclable, and malleable electronic skin enabled by dynamic covalent thermoset nanocomposite. *Sci. Adv.* **4**, eaaq0508 (2018).
11. Bang, J. et al. Highly Sensitive Temperature Sensor: Ligand-Treated Ag Nanocrystal Thin Films on PDMS with Thermal Expansion Strategy. *Adv. Funct. Mater.* **29**, 1903047 (2019).
12. Boland, C. S., Khan, U., Benameur, H. & Coleman, J. N. Surface coatings of silver nanowires lead to effective, high conductivity, high-strain, ultrathin sensors. *Nanoscale* **9**, 18507–18515 (2017).
13. Cui, Z., Poblete, F. R. & Zhu, Y. Tailoring the Temperature Coefficient of Resistance of Silver Nanowire Nanocomposites and their Application as Stretchable Temperature Sensors. *ACS Appl. Mater. Interfaces* **11**, 17836–17842 (2019).
14. Cai, Y. et al. Stretchable Ti3C2Tx MXene/Carbon Nanotube Composite Based Strain Sensor with Ultrahigh Sensitivity and Tunable Sensing Range. *ACS Nano* **12**, 56–62 (2018).
15. Qu, M. et al. Biocompatible, Flexible Strain Sensor Fabricated with Polydopamine-Coated Nanocomposites of Nitrile Rubber and Carbon Black. *ACS Appl. Mater. Interfaces* **12**, 42140–42152 (2020).
16. Lee, J. et al. Ultrasensitive Strain Sensor Based on Separation of Overlapped Carbon Nanotubes. *Small* **15**, 1–7 (2019).
17. Wang, Y., Wang, Y. & Yang, Y. Graphene–Polymer Nanocomposite-Based Redox-Induced Electricity for Flexible Self-Powered Strain Sensors. *Adv. Energy Mater.* **8**, 1–9 (2018).
18. Yang, Y. et al. A laser-engraved wearable sensor for sensitive detection of uric acid and tyrosine in sweat. *Nat. Biotechnol.* **38**, 217–224 (2019).
19. Zhang, F. et al. Multi-modal strain and temperature sensor by hybridizing reduced graphene oxide and PEDOT:PSS. *Compos. Sci. Technol.* **187**, 107959 (2020).
20. Wang, Q. et al. Self-Healable Multifunctional Electronic Tattoos Based on Silk and Graphene. *Adv. Funct. Mater.* **29**, 1808695 (2019).
21. Oh, J. et al. Pressure insensitive strain sensor with facile solution-based process for tactile sensing applications. *ACS Nano* **12**, 7546–7553 (2018).
22. Yang, Y., Shi, L., Cao, Z., Wang, R. & Sun, J. Strain Sensors with a High Sensitivity and a Wide Sensing Range Based on a Ti3C2Tx (MXene) Nanoparticle–Nanosheet Hybrid Network. *Adv. Funct. Mater.* **29**, 1807882 (2019).
23. Boland, C. S. et al. Sensitive, high-strain, high-rate bodily motion sensors based on graphene-rubber composites. *ACS Nano* **8**, 8819–8830 (2014).
24. Li, X. et al. Stretchable and highly sensitive graphene-on-polymer strain sensors. *Sci. Rep.* **2**, 1–6 (2012).
25. Kim, J. H., Kim, S. R., Kil, H. J., Kim, Y. C. & Park, J. W. Highly Conformable, Transparent Electrodes for Epidermal Electronics. *Nano Lett.* **18**, 4531–4540 (2018).

26. Bihar, E. et al. Inkjet-Printed PEDOT:PSS Electrodes on Paper for Electrocardiography. *Adv. Healthc. Mater.* **6**, 1601167 (2017).
27. Sinha, S. K. et al. Screen-Printed PEDOT:PSS Electrodes on Commercial Finished Textiles for Electrocardiography. *ACS Appl. Mater. Interfaces* **9**, 37524–37528 (2017).
28. Luo, J. et al. Pillared MXene with Ultralarge Interlayer Spacing as a Stable Matrix for High Performance Sodium Metal Anodes. *Adv. Funct. Mater.* **29**, 1–12 (2019).
29. Xiao, Z., Yang, Z., Li, Z., Li, P. & Wang, R. Synchronous Gains of Areal and Volumetric Capacities in Lithium-Sulfur Batteries Promised by Flower-like Porous Ti3C2Tx Matrix. *ACS Nano* **13**, 3404–3412 (2019).
30. Persson, I. et al. 2D Transition Metal Carbides (MXenes) for Carbon Capture. *Adv. Mater.* **31**, 1–5 (2019).
31. Shahzad, F. et al. Electromagnetic interference shielding with 2D transition metal carbides (MXenes). *Science* **353**, 1137–1140 (2016).
32. Shi, X. et al. Bioinspired Ultrasensitive and Stretchable MXene-Based Strain Sensor via Nacre-Mimetic Microscale 'brick-and-Mortar' Architecture. *ACS Nano* **13**, 649–659 (2019).
33. Wang, Y. et al. Low-cost, μm-thick, tape-free electronic tattoo sensors with minimized motion and sweat artifacts. npj Flex. *Electron* **2**, 6 (2018).
34. Hua, Q. et al. Skin-inspired highly stretchable and conformable matrix networks for multifunctional sensing. *Nat. Commun.* **9**, 244 (2018).
35. Chhetry, A. et al. Black Phosphorus@Laser-Engraved Graphene Heterostructure-Based Temperature–Strain Hybridized Sensor for Electronic-Skin Applications. *Adv. Funct. Mater.* **31**, 1–14 (2021).
36. Liu, H. et al. A Flexible Multimodal Sensor That Detects Strain, Humidity, Temperature, and Pressure with Carbon Black and Reduced Graphene Oxide Hierarchical Composite on Paper. *ACS Appl. Mater. Interfaces* **11**, 40613–40619 (2019).
37. Kaidarova, A. et al. Wearable multifunctional printed graphene sensors. npj Flex. *Electron* **3**, 15 (2019).
38. Chen, C. et al. Charge transfer induced polymerization of EDOT confined between 2D titanium carbide layers. *J. Mater. Chem. A* **5**, 5260–5265 (2017).
39. Boota, M. et al. Pseudocapacitive Electrodes Produced by Oxidant-Free Polymerization of Pyrrole between the Layers of 2D Titanium Carbide (MXene). *Adv. Mater.* **28**, 1517–1522 (2016).
40. Vahidmohammadi, A. et al. Thick and freestanding MXene/PANI pseudocapacitive electrodes with ultrahigh specific capacitance. *J. Mater. Chem. A* **6**, 22123–22133 (2018).
41. Zang, J. et al. Template-free electrochemical synthesis of superhydrophilic polypyrrole nanofiber network. *Macromolecules* **41**, 7053–7057 (2008).
42. Halim, J. et al. Transparent conductive two-dimensional titanium carbide epitaxial thin films. *Chem. Mater.* **26**, 2374–2381 (2014).
43. Bai, S. et al. Solution processed fabrication of silver nanowire-MXene@PEDOT: PSS flexible transparent electrodes for flexible organic light-emitting diodes. Compos. *Part A Appl. Sci. Manuf.* **139**, 106088 (2020).
44. Li, S. et al. Modifying Reduced Graphene Oxide by Conducting Polymer Through a Hydrothermal Polymerization Method and its Application as Energy Storage Electrodes. *Nanoscale Res. Lett.* **14**, 226 (2019).
45. Zhou, H. et al. A facile approach towards chemical modification of Ag nanowires by PEDOT as a transparent electrode for organic solar cells. *J. Mater. Chem. C.* **6**, 312–319 (2018).
46. Zhao, L., Wang, K., Wei, W., Wang, L. & Han, W. High-performance flexible sensing devices based on polyaniline/MXene nanocomposites. *InfoMat* **1**, 407–416 (2019).
47. Weng, G. M. et al. Layer-by-Layer Assembly of Cross-Functional Semi-transparent MXene-Carbon Nanotubes Composite Films for Next-Generation Electromagnetic Interference Shielding. *Adv. Funct. Mater.* **28**, 1–9 (2018).
48. Yang, Y., Shi, L., Cao, Z., Wang, R. & Sun, J. Strain Sensors with a High Sensitivity and a Wide Sensing Range Based on a Ti3C2Tx (MXene) Nanoparticle–Nanosheet Hybrid Network. *Adv. Funct. Mater.* **29**, 1–10 (2019).
49. Shi, X., Liu, S., Sun, Y., Liang, J. & Chen, Y. Lowering Internal Friction of 0D–1D–2D Ternary Nanocomposite-Based Strain Sensor by Fullerene to Boost the Sensing Performance. *Adv. Funct. Mater.* **28**, 1800850 (2018).
50. Zahed, M. A. et al. Flexible and robust dry electrodes based on electroconductive polymer spray-coated 3D porous graphene for long-term electrocardiogram signal monitoring system. *Carbon* **165**, 26–36 (2020).
51. Acar, G. et al. Wearable and flexible textile electrodes for biopotential signal monitoring: A review. *Electronics* **8**, 1–25 (2019).
52. Zhang, L. et al. Fully organic compliant dry electrodes self-adhesive to skin for long-term motion-robust epidermal biopotential monitoring. *Nat. Commun.* **11**, 1–13 (2020).
53. Koo, J. H. et al. Wearable Electrocardiogram Monitor Using Carbon Nanotube Electronics and Color-Tunable Organic Light-Emitting Diodes. *ACS Nano* **11**, 10032–10041 (2017).
54. Zhang, S. et al. A wearable battery-free wireless and skin-interfaced microfluidics integrated electrochemical sensing patch for on-site biomarkers monitoring in human perspiration. *Biosens. Bioelectron.* **175**, 112844 (2021).
55. Chhetry, A. et al. MoS2-Decorated Laser-Induced Graphene for a Highly Sensitive, Hysteresis-free, and Reliable Piezoresistive Strain Sensor. *ACS Appl. Mater. Interfaces* **11**, 22531–22542 (2019).
56. Gong, S. et al. Highly Stretchy Black Gold E-Skin Nanopatches as Highly Sensitive Wearable Biomedical Sensors. *Adv. Electron. Mater.* **1**, 1400063 (2015).

ACKNOWLEDGEMENTS

This research was funded and conducted under the Competency Development Program for Industry Specialists of the Korean Ministry of Trade, Industry and Energy (MOTIE), operated by Korea Institute for Advancement of Technology (KIAT). (No. P0002397, HRD program for Industrial Convergence of Wearable Smart Devices), and the Technology Innovation Program (20000773, Development of nanomultisensors based on wearable patch for nonhaematological monitoring of metabolic syndrom) funded by the Ministry of Trade, Industry & Energy (MI, Korea). The authors are grateful to the group members of the Advanced Sensor and Energy Research (ASER) Laboratory of Kwangwoon University for their valuable suggestions and support.

AUTHOR CONTRIBUTIONS

Conceptualization: S.Z., A.C. Methodology: S.Z., A.C. Investigation: S.Z., A.C., M.A.Z., S.S. Visualization: S.Z., A.C., M.A.Z., S.S., C.P., S.Y. Supervision: J.Y.P. Writing—original draft: S.Z., A.C. Writing—review & editing: A.C., J.Y.P.

COMPETING INTERESTS

The authors declare no competing interests.

ADDITIONAL INFORMATION

Supplementary information The online version contains supplementary material available at https://doi.org/10.1038/s41528-022-00140-4.

Correspondence and requests for materials should be addressed to Jae Y. Park.

Reprints and permission information is available at http://www.nature.com/reprints

Publisher's note Springer Nature remains neutral with regard to jurisdictional claims in published maps and institutional affiliations.